applied sciences

MDPI

Article

A Numerical Analysis of the Nonlinear Dynamics of Shimmed Conical Gas Foil Bearings

Marian Sarrazin and Robert Liebich *

Department for Engineering Design and Product Reliability, Technische Universität Berlin (TU Berlin), Str. d. 17. Juni 135, 10623 Berlin, Germany; m.sarrazin@tu-berlin.de

* Correspondence: robert.liebich@tu-berlin.de

Abstract: Conical gas foil bearings (CGFBs) have the potential to halve the number of necessary bearings in a conventional rotor system supported by gas foil bearings. Transient simulations of gas foil journal bearings and gas foil thrust bearings have proven their necessity to accurately predict the safe operating range of such bearings. This work presents the first transient model able to simulate the three-dimensional dynamics of CGFBs. The static behaviour of a single CGFB with a uniform bearing clearance is compared to a CGFB modified by thin metal shims and the resulting advantages of shimmed CGFBs are discussed. An investigation of the linear stability behaviour shows that the axial load of the bearing determines the stability of the equilibrium position. Furthermore, three transient simulations demonstrate the capability of the presented model to describe the nonlinear dynamics of a shimmed CGFB such as the occurrence of stable limit cycles and self-excited sub- and super-synchronous vibrations with and without a rotor unbalance. Additionally, waterfall diagrams are used to investigate the frequency response for different rotational speeds. The novel findings of this work are the importance of a non-uniform bearing clearance for the functionality of a CGFB and the identification of the axial force as a critical factor in maintaining bearing stability. These findings are specific to CGFBs and have not been discussed or mentioned in previous works.

Keywords: conical gas foil bearing; transient simulation; nonlinear dynamics; shimming

check for updates

Citation: Sarrazin, M.; Liebich, R. A Numerical Analysis of the Nonlinear Dynamics of Shimmed Conical Gas Foil Bearings. *Appl. Sci.* **2023**, *13*, 5859. https://doi.org/10.3390/app13105859

Academic Editor: Jaroslav Zapoměl

Received: 4 April 2023
Revised: 25 April 2023
Accepted: 5 May 2023
Published: 9 May 2023

1. Introduction

Gas Foil Bearings (GFBs) are machine elements mainly used in oil-free turbomachinery. The major benefits of GFBs are the low drag friction, low wear, and the possibility of high-speed and high-temperature operation. These properties can be achieved while maintaining a contamination-free system due to the use of air as lubrication fluid. The latter property in particular predestines GFBs for applications where the use of oil is not acceptable, such as in air cycle machines and turbo compressors for the air supply of fuel cells. Another common application of GFBs are micro gas turbines due to the wide allowable temperature range [1–3].

A GFB is characterized by a compliant foil structure between the bearing sleeve and the rotating counterpart. The rotation of the rotor leads to an aerodynamic pressure in the air gap. This pressure distribution can fully support the rotor without physical contact between the rotor and the stationary foil structure. A classical rotor system supported by GFBs includes two gas foil journal bearings (GFJBs) and two gas foil thrust bearings (GFTBs). The GFJBs support the radial loads while the GFTBs support the rotor in the axial direction. The idea of a conical gas foil bearing (CGFB) able to support radial and axial loads simultaneously has the potential to reduce the necessary number of bearings in a rotor system by a half. This not only leads to a reduction in cost and installation space but also increases the scope of design possibilities due to the reduced complexity of the overall system.

Various types of modifications of GFBs have been presented in the literature. Dellacorte and Valco [4] provided a method to characterize these bearing types into three generations.

The aim of these modifications is to enhance the static and dynamic behaviour of GFBs. A well-known disadvantage of GFBs is the occurrence of sub-synchronous vibrations [5,6]. These vibrations occur at the onset speed of sub-synchronous vibration (OSSV) and can lead to an instability of the rotor at the onset speed of sub-synchronous instability (OSSI) [7]. A known way to enhance the dynamic performance of a GFB is to insert thin metal shims between the bearing sleeve and the foil structure. This modification yields a non-uniform clearance around the circumference of the bearing [8–12].

The numerical analysis of the dynamical behaviour of GFBs can be categorized into two different approaches. Classically, a perturbation approach based on the work of Lund [13] in 1968 is used to predict linearised bearing parameters. These parameters can then be used to calculate the OSSV. Discrepancies between this OSSV and the OSSV obtained by transient analysis have been reported [14,15]. Additionally, Bonello and Pourashraf [16] have shown the inability of Lund's method to detect certain instabilities due to the omission of state variables associated with the foil and air film domains. In 2014, Bonello and Pham [17] presented a model which allows the simultaneous solution of the governing equations. The analysis of the Jacobian of this fully coupled system of equations yields the exact OSSV as obtained by a transient nonlinear dynamic analysis. In contrast to the perturbation approach, this model can furthermore predict the nonlinear stability behaviour beyond the OSSV. Baum et al. [18] and Zhou et al. [19] showed that supercritical as well as subcritical bifurcation can occur in GFBs. While subcritical bifurcations lead to stable limit cycles (sub-synchronous vibration), supercritical bifurcations lead to unstable limit cycles which can cause instability of the rotor even before the OSSV.

Regardless of the approach, different models to capture the behaviour of the compliant foil structure have been presented [20]. A model referred to as the "simple elastic foundation model" (SEFM) has been used and adapted repeatedly [17,21–31]. It provides a linear stiffness model and considers equivalent viscous damping by including a loss factor. One of the biggest flaws of the SEFM is the modelling of dissipation due to friction by using viscous damping. It is generally known that this representation is not adequate. Hence, a lot of models have been presented that not only provide a better modelling of friction but also include more of the nonlinear properties of the foil structure. These models include the nonlinear bump stiffness, the interaction between bumps, and the modelling of the top foil as a beam, plate, or shell element, all while modelling the friction between top foil, bump foil and bearing sleeve.

All these techniques have been applied to GFJBs or GFTBs. Although several patents for CGFBs can be found only a few research papers have been published [32–38]. In 2013, Kulkarni and Jan [32] presented an experimental work on CGFBs. A bearing with unusually large bumps was used and the experiments proved the ability of CGFBs to support radial and axial loads simultaneously. In recent studies from 2020 and 2021, Hu et al. [34–38] theoretically investigated the static and dynamic characteristics of CGFBs considering misalignment, and roundness and taper error. In these works, Lund's perturbation approach was used in combination with a nonlinear stiffness model of the compliant foil structure. In [34,38], the authors presented experimental results to verify the functionality of the presented CGFBs. These studies put the main research focus onto the compliant foil structure. They presented a foil structure model considering coulomb friction [37] and proposed guidelines for the design of bump-type CGFBs [35].

Although the transient analyses of GFJBs have proven their necessity to calculate an accurate OSSV [14,15], no transient investigation of CGFBs has yet been presented in the literature. Furthermore, transient simulations have shown that the nonlinear stability behaviour, e.g., stable, and unstable limit cycles are crucial for the accurate prediction of the safe operating range of GFBs [18,19]. The aim of this work is to present a fully coupled three-dimensional transient nonlinear dynamic model for CGFBs, able to predict the static characteristics, as well as the linear and nonlinear stability behaviour of CGFBs. The novelty of this work is the investigation of CGFBs using a fully coupled model. Neither an investigation of the static nor dynamic behaviour of CGFBs has been presented in previous works using this simulation approach.

To date, a particular phenomenon related to CGFBs has not been discussed in the literature. The governing equations presented in Section 2 yield the problem that the air film pressure is not directly coupled with the axial displacement of the rotor, if the rotor is in the radially central position. In that case, the bearing would provide no static axial force and stiffness. To solve this problem, it is common for conical oil bearings to use spiral grooves on the conical journal [39]. Inspired by that approach, this work investigates the use of thin metal shims between the bearing sleeve and bump foil. As stated, shimming is a common modification to enhance dynamic performance [8–10]. Furthermore, shimming could greatly enhance the axial load carrying capacity of CGFBs and solve the aforementioned problem.

2. Theory

Assuming a rigid outer bearing sleeve, the behaviour of GFBs is governed by three domains: the air film between the rotor and the compliant foil structure, the compliant foil structure itself and the rotor. Each of these domains can be described by its own set of differential equations. Bonello and Pham [17] presented a model to analyse the behaviour of GFJBs by coupling these three domains and solving them simultaneously. In the present work, this model is modified and applied to CGFBs. In the following section, the governing equations are presented, and the involved assumptions are explained. Figure 1 shows the relevant geometrical parameters and the used coordinates for a CGFB.

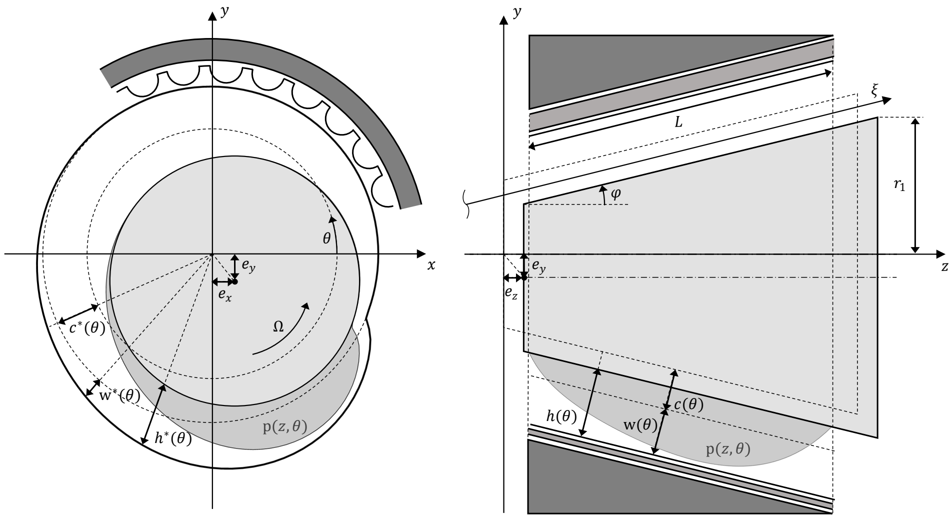

Figure 1. Geometry of a conical gas foil bearing; Parameters marked with (*) are projected onto the x-y-plane for clarity.

2.1. Fluid Film

The fluid film between the journal and the compliant foil can be described by the compressible, isothermal, isoviscous Reynolds equation. The following assumptions are commonly used to describe the behaviour of GFBs and have shown good agreement with experimental results.

1. The influence of inertia forces and the force of gravity on the fluid can be neglected.
2. The fluid flow is laminar.
3. Wall adhesion is assumed, and no-slip flow is considered.
4. The pressure is constant over the thickness of the air film.
5. The air can be described as an ideal gas.
6. The temperature of the fluid film is constant.

Assumptions 1–5 are standard for the simulation of fluid film bearings and a detailed analysis of the limitation and justification of these assumptions can be found in [40]. The assumption of a constant temperature is commonly used but partly questionable. The inclusion of a non-constant temperature greatly increases the complexity of the model and brings a lot of additional uncertainties [41]. For this reason and due to experimentally verified results of isothermal simulations, this assumption is also used for the presented model.

With these assumptions the Reynolds equation for a conical shaped air gap can be written as shown in Equation (1), where the non-dimensional pressure $\widetilde{p} = p/p_0$ and the non-dimensional film thickness $\widetilde{h} = h/c_0$ are defined by the air film pressure p, the air gap thickness h, the ambient pressure p_0 and the nominal bearing clearance c_0. For a bearing with the half-cone angle φ, a maximum radius r_1, and a length L, the coordinates $\theta \in [0, 2\pi]$ and $\zeta = \xi/\xi_1$ are defined by a coordinate $\xi \in [\xi_0, \xi_1]$ along the air gap with $\xi_1 = r_1/\sin(\varphi)$ and $\xi_0 = \xi_1 - L$. Time t is represented by dimensionless time $\tau = (\Omega/2)t$ using the angular velocity $\Omega = 2\pi n$ and the rotational speed n of the conical journal.

$$\frac{1}{\sin^2(\varphi)\zeta}\frac{\partial}{\partial\theta}\left(\widetilde{p}\widetilde{h}^3\frac{\partial\widetilde{p}}{\partial\theta}\right) + \frac{\partial}{\partial\zeta}\left(\zeta\widetilde{p}\widetilde{h}^3\frac{\partial\widetilde{p}}{\partial\zeta}\right) = \Lambda\zeta\left(\frac{\partial\widetilde{p}\widetilde{h}}{\partial\theta} + \frac{\partial\widetilde{p}\widetilde{h}}{\partial\tau}\right) \tag{1}$$

The bearing number $\Lambda = \frac{6\mu\Omega\xi_1^2}{p_0c_0^2}$ includes the viscosity μ of air. This equation can be derived from the generalized Reynold's equation presented by Kim et al. [42]. The stationary form of this equation was also presented by Agrawal [43] in 1993 and used by Hu et al. [34–38]. To the authors knowledge this equation has not yet been used for transient simulations of CGFBs or integrated into a fully coupled GFB system.

The introduction of the new state variable $\psi = \widetilde{p}\widetilde{h}$ yields Equation (2), and allows the transformation into a form which enables a simultaneous solution of the three domains.

$$\frac{\partial\psi}{\partial\tau} = \frac{1}{\Lambda\zeta}\left\{\frac{1}{\sin^2(\varphi)\zeta}\frac{\partial}{\partial\theta}\left[\psi\left(\widetilde{h}\frac{\partial\psi}{\partial\theta} - \psi\frac{\partial\widetilde{h}}{\partial\theta}\right)\right] + \frac{\partial}{\partial\zeta}\left[\zeta\psi\left(\widetilde{h}\frac{\partial\psi}{\partial\zeta} - \psi\frac{\partial\widetilde{h}}{\partial\zeta}\right)\right]\right\} - \frac{\partial\psi}{\partial\theta} \tag{2}$$

With the commonly used assumption of a constant film height in the axial direction applied Equation (2) can be simplified to Equation (3).

$$\frac{\partial\psi}{\partial\tau} = \frac{1}{\Lambda\zeta}\left\{\frac{1}{\sin^2(\varphi)\zeta}\frac{\partial}{\partial\theta}\left[\psi\left(\widetilde{h}\frac{\partial\psi}{\partial\theta} - \psi\frac{\partial\widetilde{h}}{\partial\theta}\right)\right] + \frac{\partial}{\partial\zeta}\left(\zeta\psi\widetilde{h}\frac{\partial\psi}{\partial\zeta}\right)\right\} - \frac{\partial\psi}{\partial\theta} \tag{3}$$

2.2. Foil Structure

In this work, the SEFM is applied for CGFB. The SEFM uses a linear stiffness and assumes viscous damping realised by a loss factor. The used model assumes a constant deformation of the foil structure in the axial direction. The interaction between bumps and the influence of the top foil is neglected. The SEFM has been used in many papers and has shown benefits regarding computing time. The used assumptions have been investigated in various papers and have been found to be mostly acceptable. Although the feasibility of the SEFM for CGFBs is questionable due to the possibility of a non-uniform stiffness in the axial direction, it is used to provide a runtime efficient solution.

The SEFM can describe the velocity of the foil deformation as shown in Equation (4) where the non-dimensional foil deformation is given by $\widetilde{w} = w/c_0$.

$$\frac{\partial\widetilde{w}}{\partial\tau} = \frac{2}{\eta}\left(\frac{\widetilde{p}_g}{\widetilde{k}_b} - \widetilde{w}\right) \tag{4}$$

Equation (4) uses the non-dimensional mean pressure along the bearing length $\widetilde{p}_g$ and the non-dimensional foil stiffness $\widetilde{k}_b = (k_b c_0)/p_a$ with the foil stiffness per unit area k_b. The unit of k_b is N/m^3. Together with an area A this yields a stiffness $k_b A$ with the expected unit of a mechanical stiffness N/m. The loss factor η is used to introduce viscous damping into the foil structure. Due to the necessary conversion of hysteretic damping to viscous damping, the assumption of a reference vibration frequency is required. Typically, the rotational speed Ω is used for this which yields the equivalent viscous damping coefficient per unit area $c_{\mathrm{D}} = k_{\mathrm{b}}\eta/\Omega$. This equivalent viscous damping coefficient yields a viscous damping force F_{D} of the form $F_{\mathrm{D}} = c_{\mathrm{D}}A \cdot \partial w/\partial\tau$. Correlations with experiments have shown that the effect of this assumption for nonlinear analysis of sub-synchronous vibration is not significant in most cases [30,31].

2.3. Rotor System

The equations of motion of the rotor can be derived from the single mass 3-DOF oscillator. The gravitational force $F_{\mathrm{G}} = -m_{\mathrm{r}}g$ is acting in the y-direction, the unbalance force of the rotor in the x- and y-direction and an external axial force F_{ax} is considered in the z-direction. With the rotor mass m_{r}, the rotor unbalance u, the fluid film forces $F_{\mathrm{x,y,z\,F}}$ and the non-dimensional rotor displacements $\varepsilon_{\mathrm{x,y,z}} = (e_{\mathrm{x}}, e_{\mathrm{y}}, e_{\mathrm{z}})/c_0$ the equations of motion are shown in Equation (5).

$$\frac{\partial^2}{\partial\tau^2}\begin{bmatrix}\varepsilon_{\mathrm{x}}\\ \varepsilon_{\mathrm{y}}\\ \varepsilon_{\mathrm{z}}\end{bmatrix} = \frac{4}{m_{\mathrm{r}}c_0\Omega^2}\begin{bmatrix}F_{\mathrm{xF}} + m_{\mathrm{r}}\Omega^2 u\cos(2\tau)\\ F_{\mathrm{yF}} + F_{\mathrm{G}} + m_{\mathrm{r}}\Omega^2 u\sin(2\tau)\\ F_{\mathrm{zF}} - F_{\mathrm{ax}}\end{bmatrix} \tag{5}$$

2.4. Coupling of the Domains

The fluid film and foil structure domains are coupled through the film height. The film height can be calculated from the nominal clearance, the displacement of the rotor and the deformation of the foil structure.

$$\widetilde{h}(\theta) = \frac{c(\theta)}{c_0} - \cos(\varphi)\cos(\theta)\varepsilon_{\mathrm{x}} - \cos(\varphi)\sin(\theta)\varepsilon_{\mathrm{y}} + \sin(\varphi)\varepsilon_{\mathrm{z}} + \widetilde{w} \tag{6}$$

The nominal clearance is equal around the circumference of the conical bearing but can be modified by using shims between the bearing sleeve and the bump foil. In this work the modified nominal clearance $c(\theta)$, due to the use of three shims with the thickness t_{s}, is described by Equation (7) (see ref. [9]).

$$c(\theta) = c_0 - \frac{t_{\mathrm{s}}}{2}(1 + \cos(3\,\theta)) \tag{7}$$

The movement of the rotor described by Equation (5) is coupled with the Reynolds equation (Equation (3)) through the fluid film forces $F_{\mathrm{x,y,z\,F}}$ resulting from the pressure distribution in the air gap.

$$\begin{bmatrix}F_{\mathrm{xF}}\\ F_{\mathrm{yF}}\\ F_{\mathrm{zF}}\end{bmatrix} = \begin{bmatrix}-\sin(\varphi)\cos(\varphi)\\ -\sin(\varphi)\cos(\varphi)\\ \sin^2(\varphi)\end{bmatrix} p_{\mathrm{a}}\zeta_1^2 \int_{\zeta=\zeta_0}^{\zeta_1}\int_{\theta=0}^{2\pi}\left(\frac{\psi}{\widetilde{h}} - 1\right)\begin{bmatrix}\cos(\theta)\\ \sin(\theta)\\ 1\end{bmatrix}\mathrm{d}\theta\mathrm{d}\zeta \tag{8}$$

These equations yield the problem mentioned in the introduction. For a rotor without a radial displacement and with a uniform bearing clearance, Equation (6) yields the partial derivative $\frac{\partial\widetilde{h}}{\partial\theta} = 0$. Assuming an ambient pressure in the bearing clearance, the partial derivatives of the pressure yield $\frac{\partial\widetilde{p}}{\partial\theta} = 0$ and $\frac{\partial\widetilde{p}}{\partial\zeta} = 0$. This assumed state satisfies the Reynolds equation (Equation (1)). In this case, the rotational speed of the rotor does not lead to an increase of stationary pressure in the bearing clearance independent of an axial displacement and the bearing can therefore not provide any axial support.

2.5. Numerical Solution

To solve this coupled system of differential equations, different approaches can be used. The use of finite difference method (FDM), finite element method and Galerkin reductions have been shown to be applicable. In this work, the FDM is used to approximate the derivatives in Equation (3).

Equation (3) can be converted into a form where the derivatives only occur separated from each other.

$$\frac{\partial \psi}{\partial \tau} = \frac{1}{\Lambda \zeta}\left[\frac{1}{\sin^2(\varphi)\zeta}\left(\psi\widetilde{h}\frac{\partial^2\psi}{\partial\theta^2} - \psi\psi\frac{\partial^2\widetilde{h}}{\partial\theta^2} + h\frac{\partial\psi}{\partial\theta}\frac{\partial\psi}{\partial\theta} - \frac{\partial\widetilde{h}}{\partial\theta}\psi\frac{\partial\psi}{\partial\theta}\right) + \zeta\psi\widetilde{h}\frac{\partial^2\psi}{\partial\zeta^2} + \zeta\widetilde{h}\frac{\partial\psi}{\partial\zeta}\frac{\partial\psi}{\partial\zeta} + \psi\widetilde{h}\frac{\partial\psi}{\partial\zeta}\right] - \frac{\partial\psi}{\partial\theta} \tag{9}$$

The FDM is applied to approximate the first and second-order derivatives in Equation (9) by using the central difference formulations shown in Equation (10) where f is ψ or $\widetilde{w}$ and ν is ζ or θ, respectively. The error of these approximations is of order $(\Delta\nu)^2$. To calculate the central differences a $N_z \cdot N_\theta$ FD-grid in shape of the air gap of the CGFB is used. The axial bearing edges are excluded from the grid.

$$\left.\frac{\partial f}{\partial \nu}\right|_{f=f_{i,j}} = \frac{f_{i,j+1} - f_{i,j-1}}{2\Delta\nu};\ \left.\frac{\partial^2 f}{\partial \nu^2}\right|_{f=f_{i,j}} = \frac{f_{i,j+1} - 2f_{i,j} + f_{i,j-1}}{\Delta\nu^2} \tag{10}$$

The boundary condition at the bearing edges is enforced by including $\widetilde{p} = 1$ in the central differences of the outer grid points as illustrated in Figure 2. In circumferential direction, a periodic boundary condition is used. The commonly used Guembel condition is applied by setting sub-ambient pressure to ambient pressure while integrating within Equation (8). The integrals are approximated by applying the trapezoidal rule on the FD-grid.

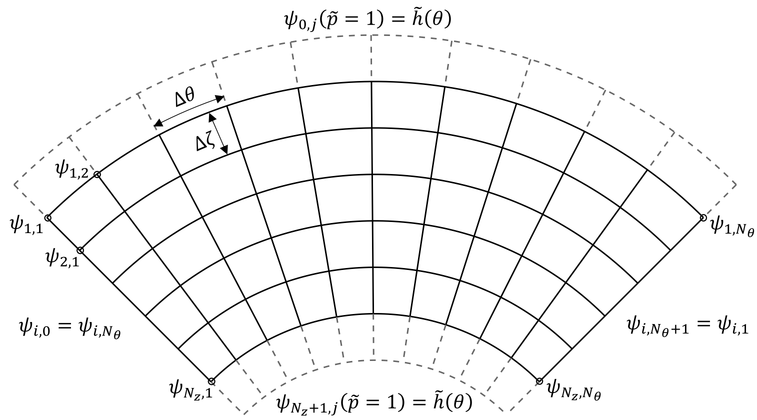

Figure 2. FD-grid of the unwound conical air gap with a representation of the used boundary conditions.

Equation (5) can be rewritten as the equivalent system of first order differential equations shown in Equation (11).

$$\frac{\partial}{\partial\tau}\begin{bmatrix}\begin{pmatrix}\varepsilon_x\\ \varepsilon_y\\ \varepsilon_z\end{pmatrix}\\ \frac{\partial}{\partial\tau}\begin{pmatrix}\varepsilon_x\\ \varepsilon_y\\ \varepsilon_z\end{pmatrix}\end{bmatrix} = \begin{bmatrix}\frac{\partial}{\partial\tau}\begin{pmatrix}\varepsilon_x\\ \varepsilon_y\\ \varepsilon_z\end{pmatrix}\\ \frac{4}{m_r c_0 \Omega^2}\begin{pmatrix}F_{xF} + m_r\Omega^2 u\cos(2\tau)\\ F_{yF} + F_G + m_r\Omega^2 u\sin(2\tau)\\ F_{zF} - F_{ax}\end{pmatrix}\end{bmatrix} \tag{11}$$

Substituting the FD-formulation into Equations (4) and (9) yields the vector functions $\mathbf{g}_\psi$ and $\mathbf{g}_{\widetilde{w}}$. Together with Equation (11) this results in a system of $N_\theta(N_z + 1) + 6$ coupled ordinary first order differential equations. The state vector $\mathbf{s}$ and the vector function $\mathbf{g}(\tau, \mathbf{s})$ are shown in Equation (12). The vector function $\mathbf{g}_\varepsilon$ results from Equation (11) and $\mathbf{J}$ represents the Jacobian of the dynamical system.

$$\mathbf{g}(\tau,\mathbf{s}) = \frac{\partial \mathbf{s}}{\partial \tau}; \mathbf{s} = \begin{bmatrix} \boldsymbol{\psi}_{\mathrm{FD}} \\ \widetilde{\mathbf{w}}_{\mathrm{FD}} \\ \boldsymbol{\varepsilon} \\ \frac{\partial \boldsymbol{\varepsilon}}{\partial \tau} \end{bmatrix}; \boldsymbol{\varepsilon} = \begin{bmatrix} \varepsilon_{\mathrm{x}} \\ \varepsilon_{\mathrm{y}} \\ \varepsilon_{\mathrm{z}} \end{bmatrix}; \mathbf{g}(\tau,\mathbf{s}) = \begin{bmatrix} \mathbf{g}_{\psi} \\ \mathbf{g}_{\widetilde{w}} \\ \frac{\partial \varepsilon}{\partial \tau} \\ \mathbf{g}_{\varepsilon} \end{bmatrix}; \mathbf{J} = \frac{\partial \mathbf{g}(\tau,\mathbf{s})}{\partial \mathbf{s}} \tag{12}$$

In this work, this system is solved using the *Matlab* function *fsolve* to find equilibrium positions where all time derivatives are equal to zero and the *Matlab* ODE solver *ode23s* to perform transient simulations. In both cases, an analytical formulation for the Jacobian matrix of the system is used to reduce computation time.

3. Model Comparison

According to the author's knowledge, no models for transient simulations of CGFBs have been published in the publicly available literature. Therefore, a direct numerical validation of the presented model is not possible. To investigate if the results of the present model are credible, a comparison with results from transient simulations for cylindrical GFBs is drawn. For this, the half-cone angle in the present model is set to a small value of $\varphi = 0.001°$. This allows the comparison with the results from [17,19,44]. Table 1 shows the used parameters.

Table 1. Bearing parameters and fluid properties used for the model comparison to represent a cylindrical GFB ($\varphi = 0.001°$) to allow the comparison with results for GFJB.

Ambient pressure	p_a	1.01×10^5 Pa
Viscosity of air	μ	1.95×10^{-5} Pa s
Nominal clearance	c_0	31.8×10^{-6} m
Half cone angle	φ	$0.001°$
Maximum radius	r_1	19.05×10^{-3} m
Bearing length	L	38.1×10^{-3} m
Foil stiffness	k_b	4.739×10^{18} N/m^3
Loss factor	η	0.25
Rotational speed	n	10,000 rpm
Rotor mass	m_r	3.061 kg
Rotor unbalance	$m_r u$	0 kgm

Figure 3 shows the trajectories of the rotor after starting the transient simulation from the bearing center with and without the application of the Guembel condition. The resulting trajectories are consistent with the results from [17,19,44] regardless of whether the Guembel condition is used or not. These agreements verify the correct implementation of the presented model.

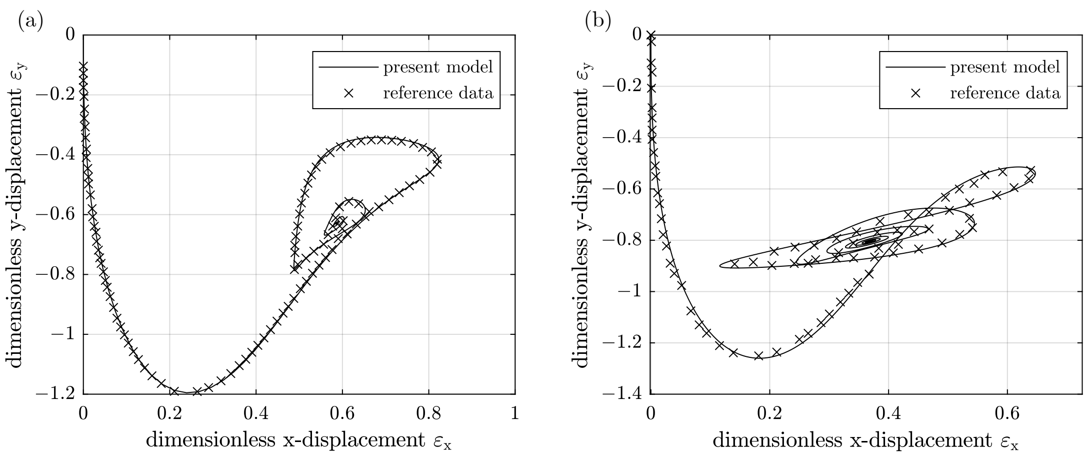

Figure 3. Trajectories after a drop from the bearing center for comparison with results from the literature without (**a**) [17] and with (**b**) [44] Guembel condition.

The shown results are calculated with a grid size of $N_\theta = 64$ and $N_z = 16$. To show the effect of the grid size, Figure 4 shows the deviation of the dimensionless y-displacement of the equilibrium position $\varepsilon_{\mathrm{yeq}}$ of the case shown in Figure 3b for different grid sizes. The maximum deviation from the calculated value is 0.14% ($N_\theta = 64, N_z = 28$). This shows that a refinement beyond $N_\theta = 64$ and $N_z = 16$ does not result in a significant change of the calculated value and therefore this grid size is used for the rest of the presented simulations.

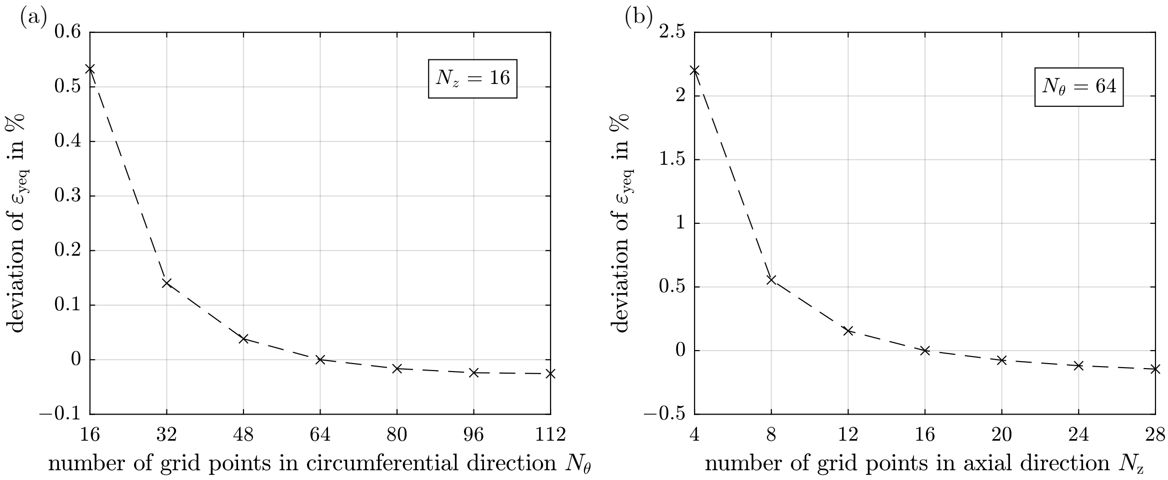

Figure 4. Deviation of the dimensionless y-displacement of the equilibrium position $\varepsilon_{\mathrm{yeq}}$ of the case shown in Figure 3b for a variation of N_θ (**a**) and N_z (**b**).

4. Results and Discussion

To demonstrate the capability of the present model a few simulation results are presented. These simulations are supposed to capture the static and dynamic, as well as the linear and nonlinear stability behaviour of CGFB. The parameters used for these investigations are shown in Table 2.

Table 2. Bearing parameters and fluid properties of a CGFB ($\varphi = 15°$).

Ambient pressure	p_{a}	1.01×10^5 Pa
Viscosity of air	μ	1.95×10^{-5} Pa s
Nominal clearance	c_0	31.8×10^{-6} m
Half cone angle	φ	15°
Maximum radius	r_1	19.05×10^{-3} m
Bearing length	L	38.1×10^{-3} m
Foil stiffness	k_{b}	4.739×10^{18} N/m^3
Loss factor	η	0.25
Rotational speed	n	10,000 rpm
Rotor unbalance	$m_{\mathrm{r}}u$	0 kgm

In the first simulation, the static performance of CGFBs is investigated. The equilibrium positions for different masses and external axial forces are calculated by setting $\mathbf{g}(\tau, \mathbf{s})$ to 0. For any bearing able to support an axial load it is crucial to provide an axial stiffness. Therefore, the axial force must increase the further the conical journal moves into the bearing. Because of the coupling of radial and axial forces in conical bearings, it is important to investigate these axial forces for a constant rotor mass which results in a constant radial force. Figure 5 shows the axial forces for different rotor masses and the corresponding axial displacement of the conical journal for a CGFB with and without the use of shims with a thickness of $t_s = 25 \times 10^{-6}$ m. It can be seen that, without shims, the axial force only slightly increases with increasing axial displacement. The axial force is mostly dependent on the rotor mass. This results in a very small range of axial force which can be provided for a constant rotor mass. If the axial force onto the bearing is too low, the bearing clearance would increase until the radial force could no longer be supported. This range of supportable axial force is a key parameter for the integration into a rotor system with two opposing conical bearings. The larger the range of a bearing, the more robust a rotor system can be designed. The strong dependency between rotor mass and axial force results in the problem mentioned in the introduction. The simulations with the mentioned simplifications show that a CGFB with a uniform bearing clearance can support no axial load without a radial force acting on the bearing. This problem can be solved by using shims to modify the bearing clearance into a nonuniform shape. The results for a shimmed CGFB in Figure 5 show that the dependency on the rotor mass can be strongly decreased while the range of supportable axial force increases. This makes a shimmed CGFB much more suitable for the use in rotor systems with two opposing CGFBs.

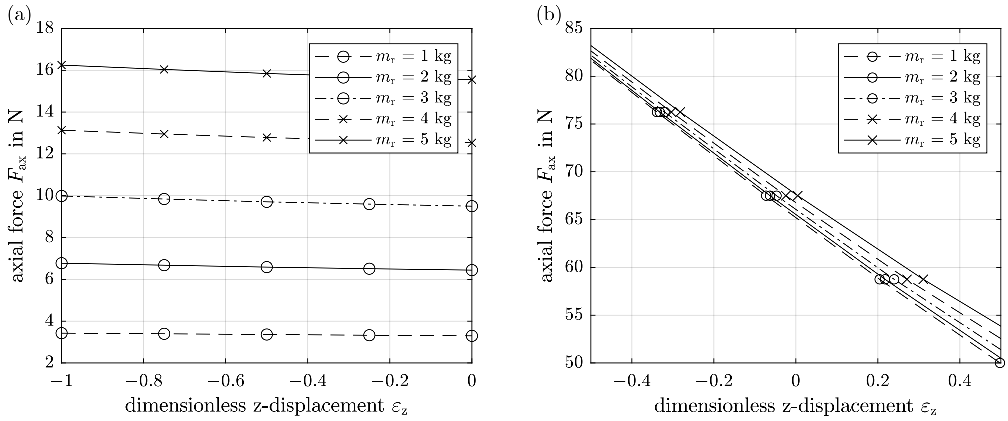

Figure 5. Axial force for different rotor masses and axial displacements for a CGFB without (**a**) and with (**b**) the use of shims.

To investigate why the shimmed and unshimmed CGFBs show such different static properties, the calculated pressure distributions in a shimmed and unshimmed CGFB on the unwound lateral surface of the conical air gap are shown in Figure 6. In order to be able to compare the pressure distributions in a meaningful way, the axial displacement of the rotor was fixed to $\varepsilon_z = -0.5$ and the same mass of $m_r = 5$ kg was used for both calculations. Without shims, one pressure maximum resulting from decreasing air gap in circumferential direction occurs. At $\theta \approx 330°$, the influence of the Guembel condition is clearly visible as the pressure at this point does not drop below one. Because only one maximum occurs only a small circumferential section is relevant for the resulting forces. Equation (8) yields that, the smaller the relevant section, the more constant the ratio between the resulting radial and axial forces becomes. This explains the strong dependency between mass and axial force in an unshimmed CGFB. Figure 7 shows the section of the pressure distribution in shimmed and unshimmed CGFB through the respective pressure maxima in circumferential and axial direction. For an unshimmed bearing, the pressure maximum is slightly shifted to the larger opening of the bearing. This is expected, due to the higher circumferential speed of the conical journal at this side.

In a shimmed CGFB, three local pressure maxima occur at the circumferential locations in each shim. Therefore, the relevant section for the resulting forces is much larger compared to an unshimmed CGFB. When calculating the radial forces, these maxima partially compensate each other, but when calculating the axial force, they add up. This explains why the coupling between rotor mass and axial force is much smaller for a shimmed bearing than for an unshimmed one. It is interesting to note that the pressure is always greater than 1 and thus the Guembel condition has no influence on the pressure distribution at this equilibrium position. The maximum pressure is slightly shifted to the smaller side of the bearing. This can be explained by the higher change of the film height resulting from the assumed modification of the bearing clearance seen in Equation (7). This effect at the smaller side of the bearing dominates the effect due to higher circumferential speed at the larger side.

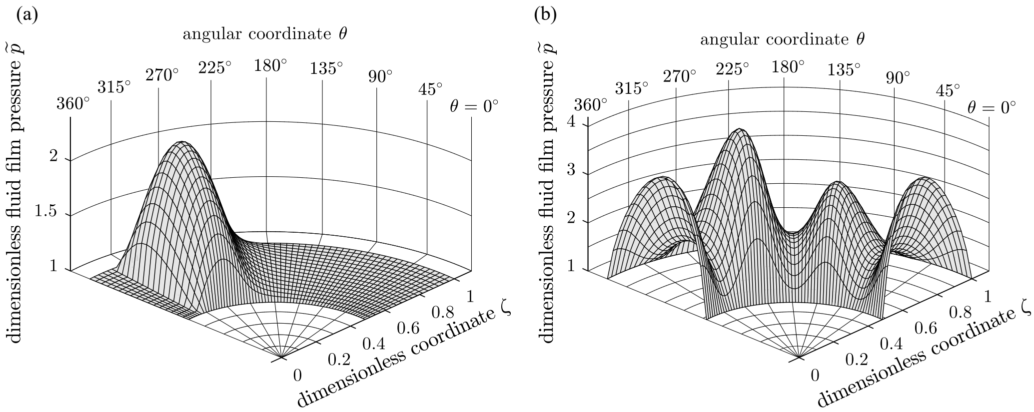

Figure 6. Pressure distribution on the unwound lateral surface of the conical air gap without (**a**) and with (**b**) shims for a rotor mass $m_\mathrm{r} = 5$ kg and axial displacement $\varepsilon_z = -0.5$.

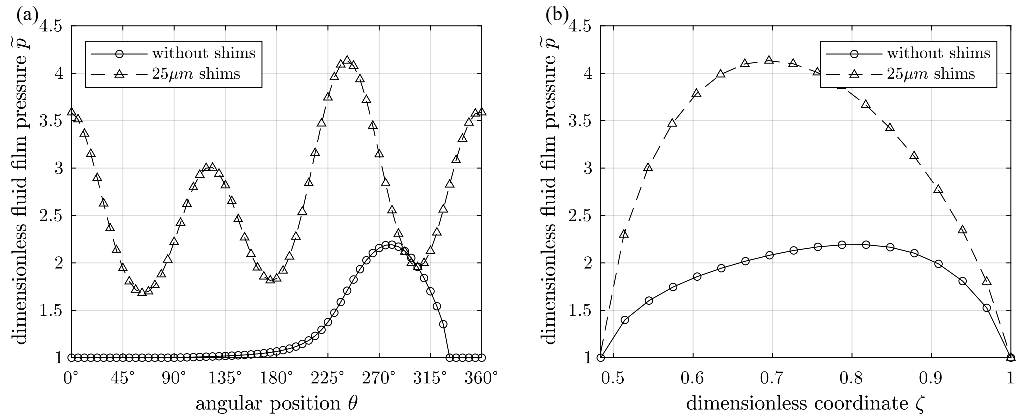

Figure 7. Section of the pressure distribution in shimmed and unshimmed CGFB through the respective pressure maxima in circumferential (**a**) and axial direction (**b**) for a rotor mass $m_\mathrm{r} = 5$ kg and axial displacement $\varepsilon_z = -0.5$.

Figures 6 and 7 show that the generated pressure inside a shimmed CGFB is much higher than in a unshimmed one. This can be explained by the additional ramps created by the shims, which generate additional pressure. As can also be seen in Figure 5, this leads to a considerably higher axial force for the same axial displacement.

The dynamic and linear stability behaviour of a CGFB can be analysed by evaluating the leading eigenvalue of the Jacobian matrix for an equilibrium position. An equilibrium position with a negative real part of the leading eigenvalue can be characterised as stable. If the real part of the eigenvalue is positive the equilibrium position is unstable. The eigenvalue analysis of the matrix $\mathbf{J}$ of an equilibrium position $\mathbf{s}_\mathrm{E}$ yields N_λ eigenvalues. The stability of the equilibrium is governed by the leading eigenvalue λ_L, which is the one with the highest real part. This yields the stability criterion shown in Equation (13).

$$\mathrm{Re}(\lambda_L) = \max\big(\mathrm{Re}(\lambda_1), ..., \mathrm{Re}(\lambda_{N_\lambda})\big) < 0 \tag{13}$$

This is a linear approach and only evaluates the stability at the equilibrium position itself and gives no information about possible stable or unstable limit cycles. Figure 8 shows the real part of the leading eigenvalue for the equilibrium positions for different axial forces and rotor masses for a shimmed CGFB. It can be seen that the axial force in particular is extremely important to guarantee a stable equilibrium point. The higher the axial force, the more stable the equilibrium position becomes. This is a interesting result because generally the axial force or the axial direction does not play an important role regarding the rotor stability. A GFJB normally becomes more stable the higher the rotor mass gets. This cannot be said for shimmed CGFBs. If the axial force is high enough to ensure a stable operation, a lower rotor mass can stabilise the rotor even more. Figure 8 also shows the stability borders for different rotational speeds. The higher the rotational speed becomes, the more axial force is needed to stabilise the bearing. It is interesting to note that for higher rotational speeds, a lower rotor mass can be beneficial for the bearing stability. Due to the small range of supportable axial forces, such stability maps cannot be calculated for unshimmed CGFBs.

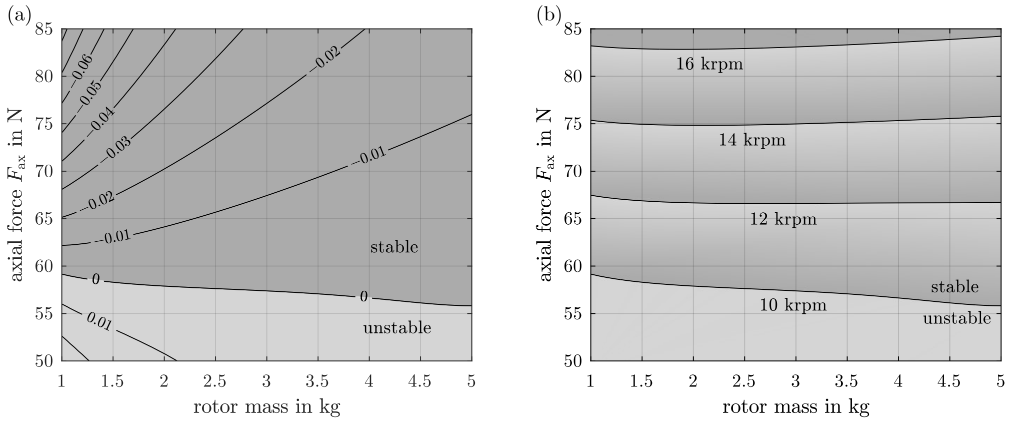

Figure 8. Real part of the leading eigenvalue of a shimmed CGFB depending on the rotor mass m_r and axial force F_{ax} of a shimmed CGFB with a rotational speed n = 10,000 rpm (**a**) and stability borders for different speeds (**b**).

To further investigate the stability behaviour of shimmed CGFBs, three transient simulations for different operating points are presented. Figure 9 shows the trajectory for a bearing with a rotor mass $m_r = 1.25$ kg, and axial load $F_{ax} = 83$ N at a rotational speed n = 10,000 rpm after a drop from the bearing center. This operating point is characterized as stable in Figure 8. The transient simulation supports this statement. The radial and axial movements of the rotor decay within the first 30 journal rotations. After that, the journal remains at an equilibrium position for the rest of the simulated time.

Transient simulations are particularly interesting for the assessment of unstable operation. In contrast to the linear stability analysis using the Jacobian matrix at the equilibrium position, a transient simulation can further characterize the nonlinear stability behaviour. Figure 10 shows the transient simulation results for an unstable operating point. The journal does not end up in a stable equilibrium position. Instead, the trajectory approaches a stable limit cycle. After around 100 rotations, the limit cycle does not change significantly for the remaining 400 simulated rotations.

Figure 11 shows the journal movement in x-, y- and z-direction and the corresponding frequency spectrum. Because of the assumption of a perfectly balanced rotor, no harmonic vibration occurs. A sub-synchronous vibration with a frequency ratio of 0.725 can be seen in all directions. Such sub-synchronous vibrations are common in nonlinear dynamic systems and are well known to occur in rotor systems supported by GFB. Furthermore, super-harmonic vibrations appear in all directions. The frequencies of these super-harmonic vibrations appear to be integer multiples of the frequency of the mentioned sub-harmonic vibration. This behaviour is common for nonlinear systems. It is noticeable that the sub-harmonic dominates in the axial direction while the first super-harmonic dominates in the x-direction. In the y-direction, the sub-harmonic and the first super-harmonic occur with almost the same amplitudes.

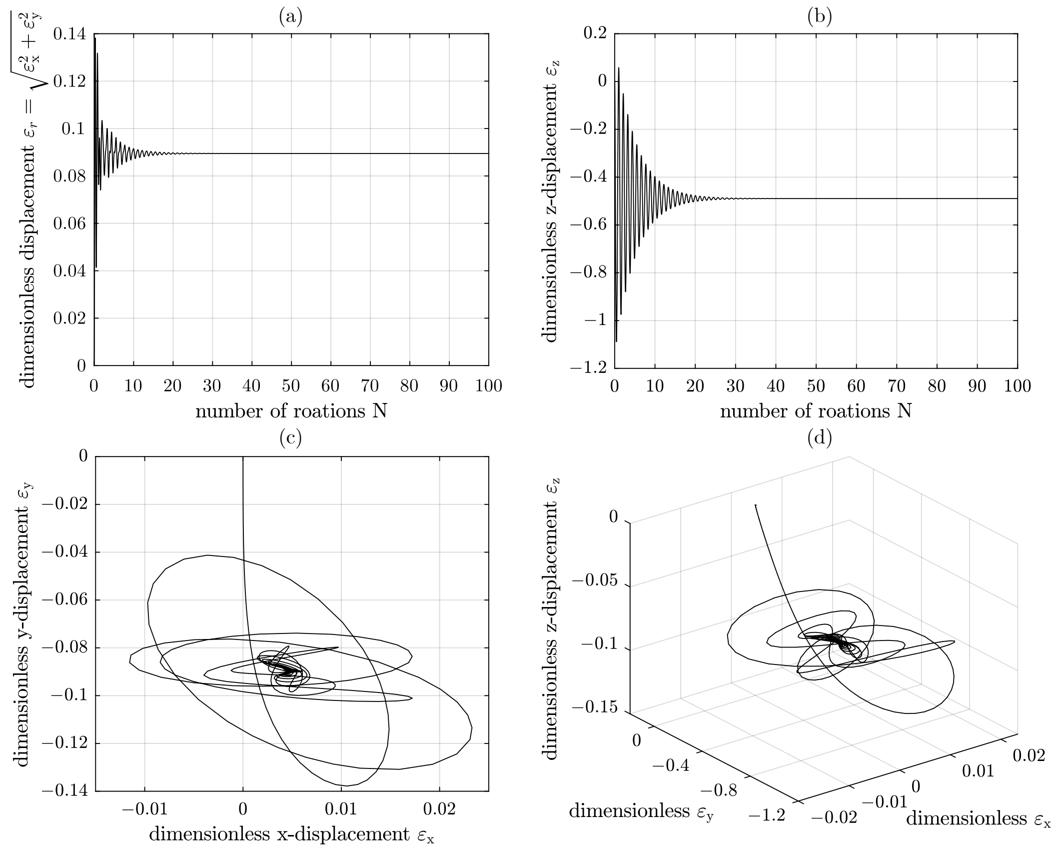

Figure 9. Trajectory and rotor movement in radial (**a**) and axial direction (**b**) after a drop from the bearing center for a rotor mass $m_r = 1.25$ kg and axial force $F_{ax} = 83$ N in a shimmed CGFB; (**c**) x-y-plane (**d**) three-dimensional trajectory.

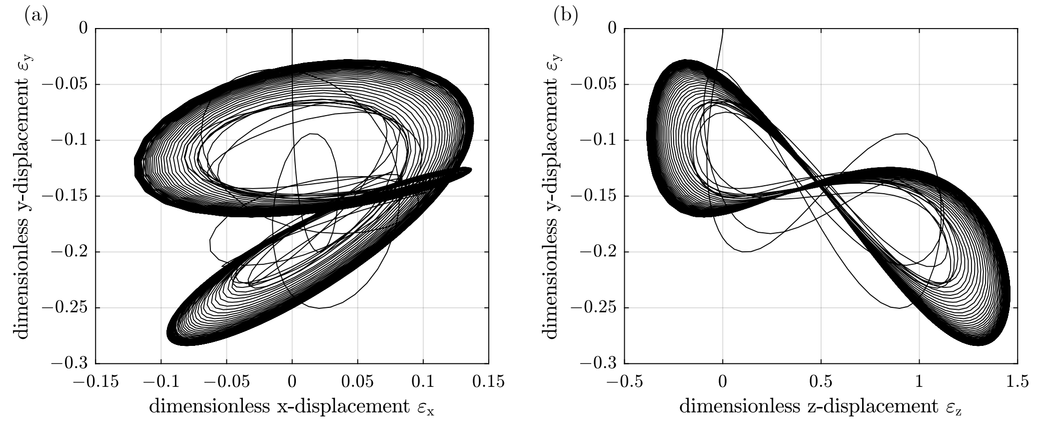

Figure 10. Trajectory after a drop from the bearing center for a rotor mass $m_r = 1.5$ kg and axial force $F_{ax} = 52$ N in a shimmed CGFB; (**a**) x-y-plane (**b**) y-z-plane.

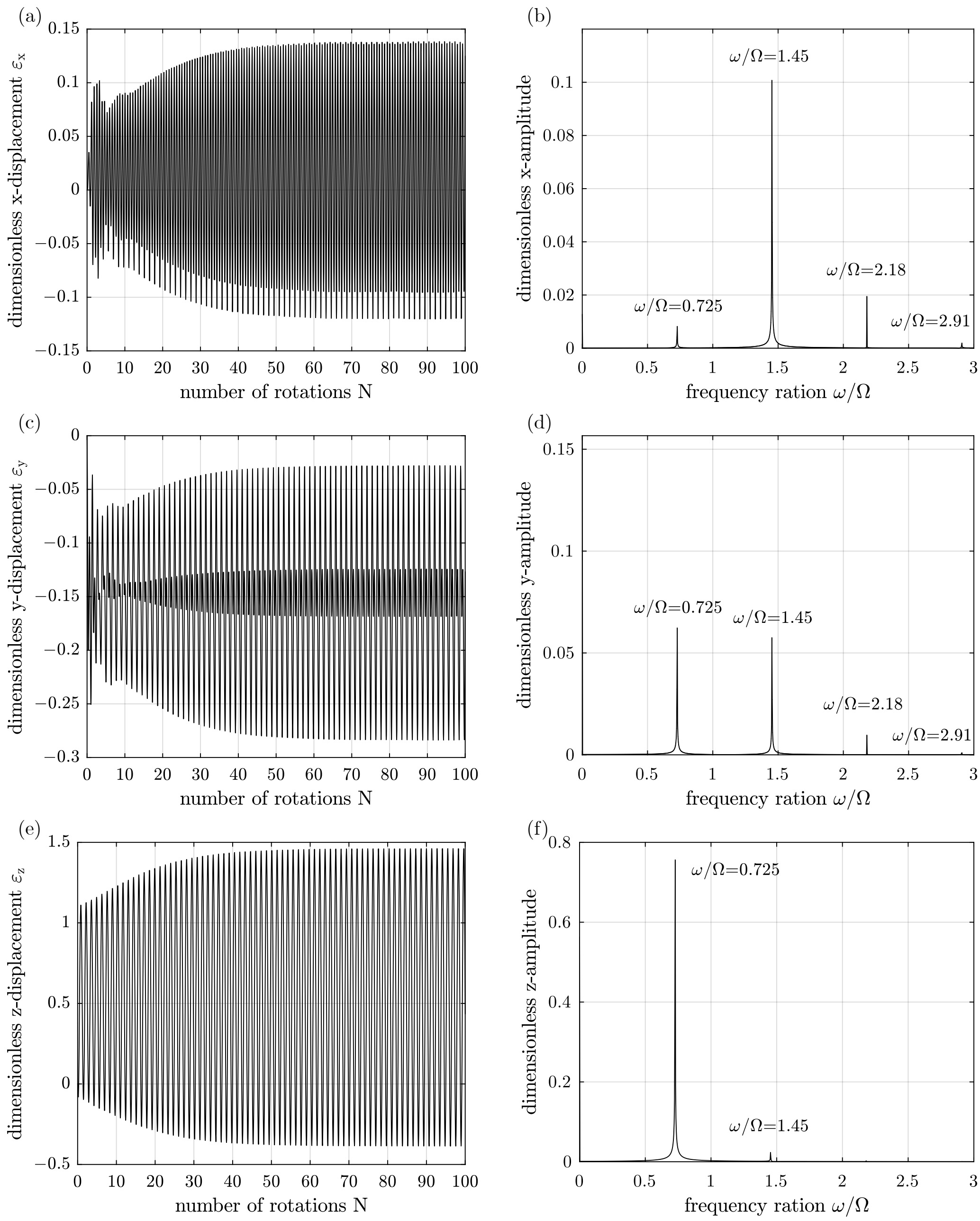

Figure 11. Rotor movement in x-, y- and z-direction in a shimmed CGFB after a drop from the bearing center for a rotor mass $m_{\mathrm{r}} = 1.5$ kg and axial force $F_{\mathrm{ax}} = 52$ N (**a**,**c**,**e**) and the corresponding frequency spectrum (**b**,**d**,**f**) of the stationary limit cycle after 100 rotations.

In addition to the shown simulation for a perfectly balanced rotor, the presented model is also capable of capturing the behaviour of an unbalanced system. Figure 12 shows the trajectory of a rotor with an unbalance of $m_{\mathrm{r}}u = 10^{-6}$ kgm. In comparison to the balanced case, a more complex trajectory occurs. After around 50 shaft rotations the maximum amplitude of the displacement does not grow further. However, no approach to a simple limit cycle, e.g., as seen in Figure 10, can be observed. Figure 13 shows the movement of the shaft in x-, y- and z-directions and the corresponding frequency spectrum. The sub- and super-harmonic vibrations observed in the case without an unbalance are still present with the same frequencies but slightly different amplitudes. In addition, the unbalance response with a frequency ratio of 1 can be seen in x- and y-direction and a few more sub- and super-harmonics occur. Two sub-harmonics and one super-harmonic with a frequency ratio of 0.272, 0.455 and 1.73 appear mostly in x-direction and y-direction. Contrary to the vibration in the perfectly balanced case, the frequencies of these sub- and super-harmonics are non-integer multiples of a lower frequency component.

To further investigate the nonlinear stability behaviour and the characteristics of the appearing limit cycles, Figure 14 shows the limit cycles of the simulations above, with and without a rotor unbalance after the first 500, for an additional 1000 shaft rotations. It could be assumed that the limit cycle of the unbalanced case is just the limit cycle from the balanced case overlain by the harmonic response to the unbalance force. However, this would not explain the additional sub- and super-synchronous vibrations mentioned above. It seems like the unbalance force not only causes a harmonic response but also excites additional sub- and super-synchronous vibrations itself. To classify the nature of these limit cycles a three-dimensional Poincaré map shown in Figure 14 can be used. In both cases, the Poincaré map shows a three-dimensional closed loop with an uncountable number of points. This classifies both limit cycles despite their different appearances as quasi periodic.

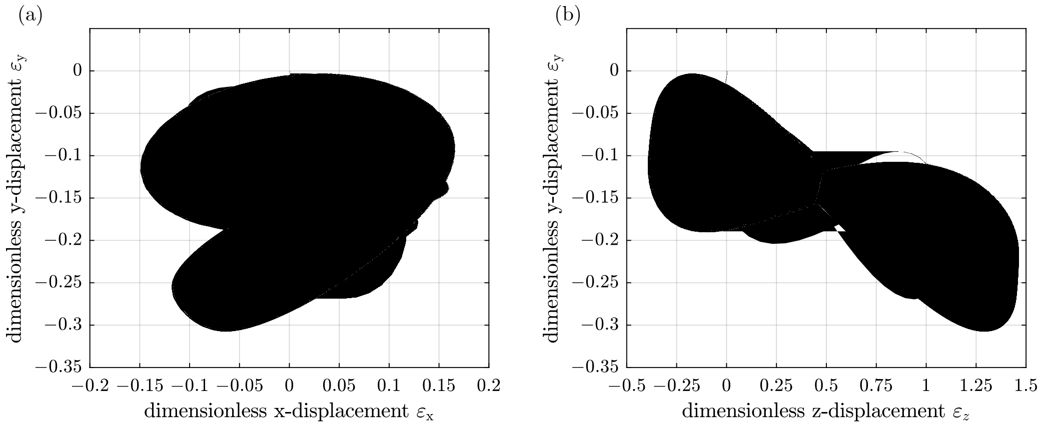

Figure 12. Trajectory after a drop from the bearing center for a rotor mass $m_{\mathrm{r}} = 1.5$ kg and axial force $F_{\mathrm{ax}} = 52$ N with a rotor unbalance $m_{\mathrm{r}}u = 10^{-6}$ kgm in a shimmed CGFB; (**a**) x-y-plane (**b**) y-z-plane.

Waterfall diagrams for the x- and z-direction with and without a rotor unbalance are presented in Figure 15. Sub- and super-harmonic vibrations as a result of instabilities can be observed. The parameters are the same as in Figures 10 and 12. These plots can be used to investigate how the different sub- and super-harmonic vibrations behave at different rotational speeds. They are constructed by calculating the frequency spectrum for different speeds from transient simulations. For every rotational speed, a transient simulation starting from the bearing center with a duration of 3 s is performed. To ensure a steady state vibration, the first second of the simulation is discarded and the remaining 2 s are used for the Fourier transform to obtain the frequency spectrum. It can be seen that in case of a perfectly balanced rotor, no harmonic vibration occurs and that the sub- and super-harmonic vibrations mainly appear after a rotational speed of 8000 rpm. The frequency of these vibrations stays almost constant for rising rotational speeds. Therefore, the frequency ratio to the harmonic changes for different speeds. As seen before in Figure 13, the dynamic behaviour becomes more complex in case a rotor unbalance is added. In the x-direction the harmonic (denoted as 1 Ω) is clearly visible. The self-excited vibrations from the case without an unbalance are still present. Additional sub- and super-harmonics appear in the x-direction. These vibrations show a different behaviour. Their frequencies do not stay constant but increase or decrease with an increasing rotational speed. These frequencies seem to change parallel to the harmonic (1 Ω) or the negative harmonic (−1 Ω).

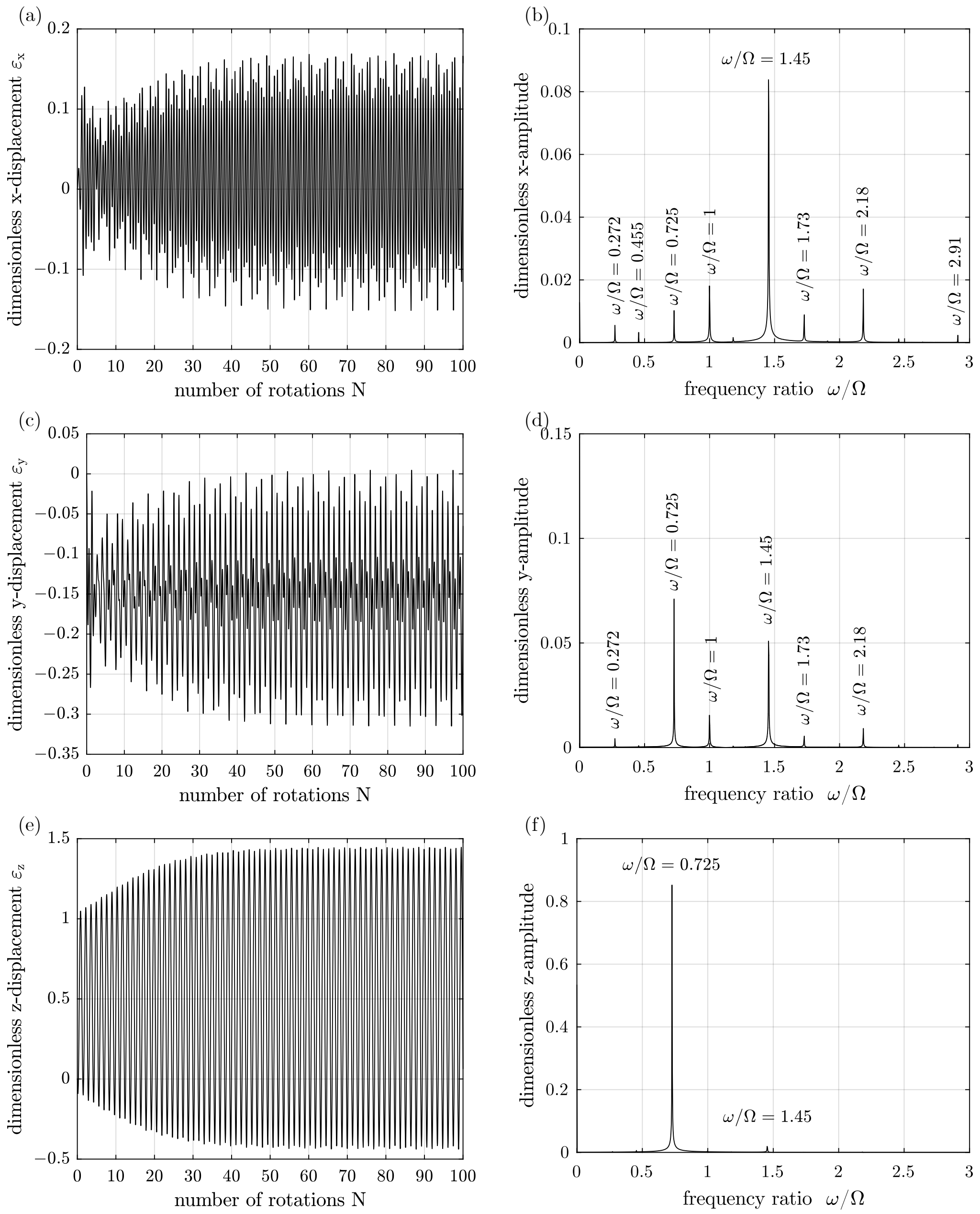

Figure 13. Rotor movement in x-, y- and z-direction in a shimmed CGFB after a drop from the bearing center for a rotor mass $m_\mathrm{r} = 1.5$ kg and axial force $F_\mathrm{ax} = 52$ N (**a**,**c**,**e**) with a rotor unbalance $m_\mathrm{r} u = 10^{-6}$ kgm and the corresponding frequency spectrum (**b**,**d**,**f**) of the stationary limit cycle after 100 rotations.

To the author's knowledge, there are no publicly available experimental results for CGFBs. As a result, it is not possible to directly validate the presented findings experimentally. However, a qualitative comparison can be made with experimental results for GFJBs. The results presented by Hoffmann and Liebich [7] for a rigid rotor supported by two GFJBs show many similarities to the presented waterfall diagram in Figure 13c. The harmonic (1 Ω), sub-harmonic vibrations with near constant frequencies, and the additional frequencies which seem to change parallel to the harmonic (1 Ω) or the negative harmonic (−1 Ω) can be found in the experimental results. Although the systems are not directly comparable, the similarities of the results indicate the credibility of the presented findings.

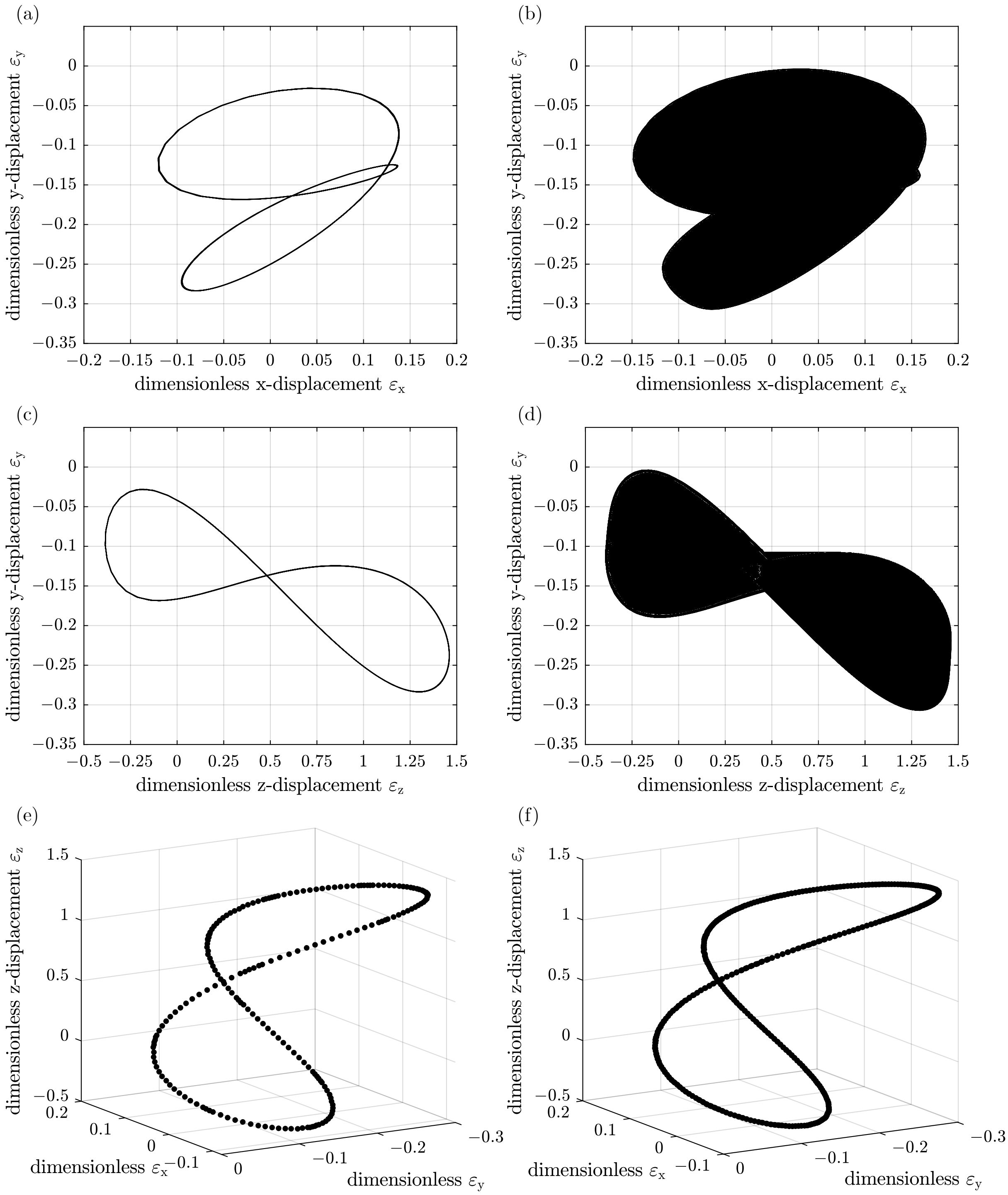

Figure 14. Stationary limit cycles in a shimmed CGFB for a rotor mass $m_r = 1.5$ kg and axial force $F_{ax} = 52$ N without (**a**,**c**,**e**) and with (**b**,**d**,**f**) a rotor unbalance $m_r u = 10^{-6}$ kgm and the corresponding Poincaré maps.

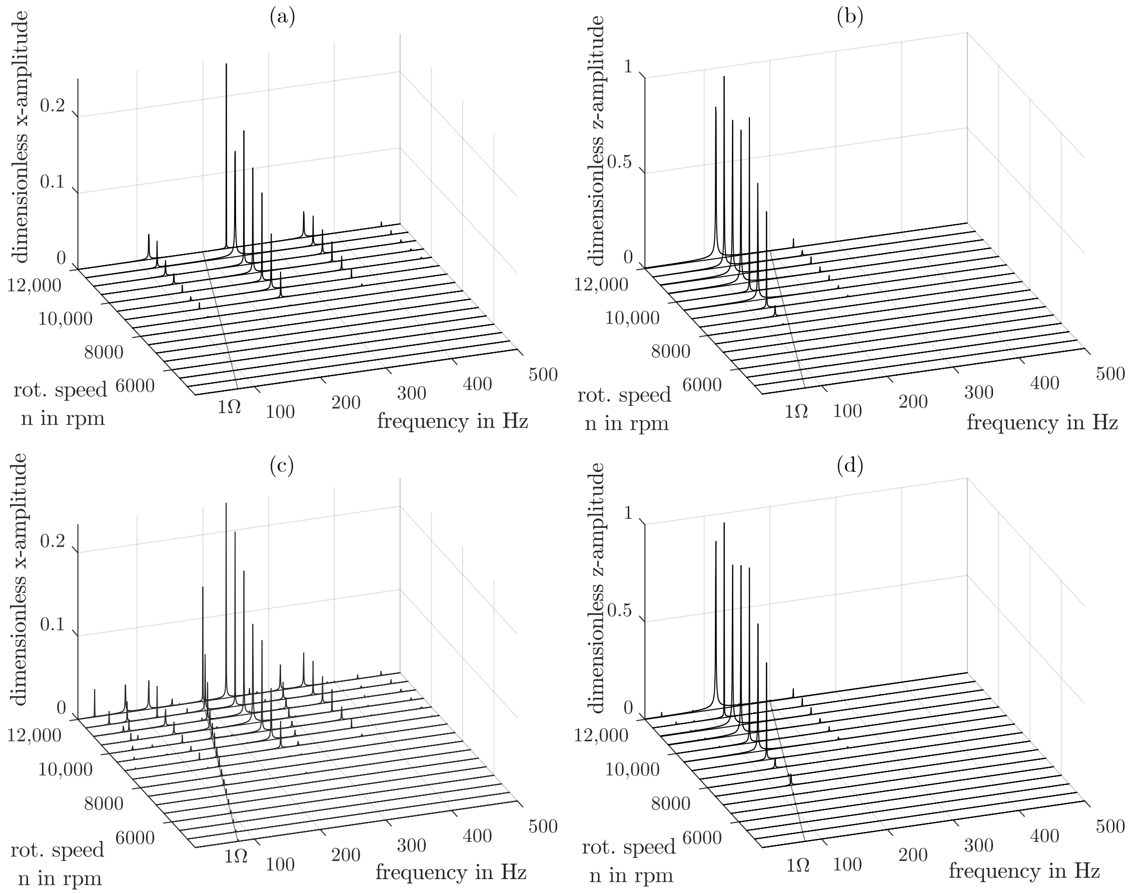

Figure 15. Waterfall diagrams for the x- and z-displacement for a rotor mass $m_\mathrm{r} = 1.5$ kg and axial force $F_\mathrm{ax} = 52$ N without (**a**,**b**) and with (**c**,**d**) a rotor unbalance $m_\mathrm{r}u = 10^{-6}$ kgm.

5. Conclusions

According to the author's knowledge, this paper presents the first transient model for CGFBs. A well-known transient model for GFJBs and GFTBs is modified and applied to CGFBs.

The results show a drastically different static behaviour depending on whether the bearing clearance is modified by shims or not. A bearing with a uniform clearance shows a strong coupling between radial load and axial force and a comparatively weak correlation between axial force and axial displacement. A shimmed CGFB shows contrary behaviour. While the axial force is strongly coupled to the axial displacement, the radial load only has a minor impact. This gives a shimmed CGFB a much greater range of supportable axial force for a constant rotor mass compared to an unshimmed bearing. For a robust rotor system, a certain range of supportable axial forces is necessary to compensate for manufacturing inaccuracies and non-constant axial loads in practical applications. This indicates that for practical use a CGFB with non-uniform bearing clearance could be much more suitable.

The results of a linear stability analysis show that especially the axial load of the bearing determines whether a stable equilibrium position occurs or not. For increasing rotational speeds, a higher axial force is necessary to stabilise the system. The first presented transient simulation shows the decaying vibrations of a perfectly balanced rotor with a stable equilibrium position. The second one captures a stable limit cycle of a perfectly balanced rotor. This limit cycle represents a self-excited sub-synchronous vibration that dominates in the axial direction. Although with much smaller amplitudes, this sub-synchronous vibration can also be seen in the radial directions. The third simulation with an added unbalance shows additional sub- and super-harmonic vibrations which are, contrary to the vibrations in the balanced case, non-integer multiples of a lower frequency component.

The presented waterfall diagrams show that above a threshold speed, self-excited vibrations occur with an almost constant frequency at increasing rotational speeds. In contrast, neither a constant frequency nor a constant frequency ratio to the harmonic is observed for the additional sub- and super-harmonic vibrations in the case of an added unbalance. These frequencies seem to change parallel to the harmonic ($1\,\Omega$) or the negative harmonic ($-1\,\Omega$).

These simulations demonstrate the capability of the presented transient model to describe the static and dynamic behaviour of shimmed CGFBs. The findings highlight the significance of a non-uniform bearing clearance and the crucial role of the axial load in maintaining bearing stability. These novel conclusions contribute to a better understanding of the underlying phenomena and can provide guidance for the design of complex rotor systems supported by CGFBs.

Author Contributions: Conceptualization, M.S.; methodology, M.S.; software, M.S.; formal analysis, M.S.; investigation, M.S.; resources, R.L.; data curation, M.S.; writing—original draft preparation, M.S.; writing—review and editing, R.L. and M.S.; visualization, M.S.; supervision, R.L.; project administration, M.S.; funding acquisition, R.L. All authors have read and agreed to the published version of the manuscript.

Funding: We acknowledge support by the German Research Foundation and the Open Access Publication Fund of TU Berlin.

Institutional Review Board Statement: Not applicable.

Informed Consent Statement: Not applicable.

Data Availability Statement: Data sharing does not apply to this article.

Conflicts of Interest: The authors declare no conflict of interest.

References

1. Agrawal, G.L. Foil Air/Gas Bearing Technology—An Overview. In Proceedings of the ASME 1997 International Gas Turbine and Aeroengine Congress and Exhibition, Orlando, FL, USA, 2 June 1997; Volume 1: Aircraft Engine; Marine; Turbomachinery; Microturbines and Small Turbomachinery; p. V001T04A006. [CrossRef]
2. Heshmat, H.; Hermel, P. Compliant Foil Bearings Technology and Their Application to High Speed Turbomachinery. In *Thin Films in Tribology: Proceedings of the 19th Leeds-Lyon Symposium on Tribology Held at the Institute of Tribology, University of Leeds*; Tribology Series; Dowson, D., Taylor, C., Childs, T., Godet, M., Dalmaz, G., Eds.; Elsevier: Leeds, UK, 1993; Volume 25, pp. 559–575. [CrossRef]
3. Hou, Y.; Zhao, Q.; Guo, Y.; Ren, X.; Lai, T.; Chen, S. Application of Gas Foil Bearings in China. *Appl. Sci.* **2021**, *11*, 6210. [CrossRef]
4. Dellacorte, C.; Valco, M.J. Load Capacity Estimation of Foil Air Journal Bearings for Oil-Free Turbomachinery Applications. *Tribol. Trans.* **2000**, *43*, 795–801. [CrossRef]
5. Heshmat, H. Advancements in the Performance of Aerodynamic Foil Journal Bearings: High Speed and Load Capability. *J. Tribol.* **1994**, *116*, 287–294. [CrossRef]
6. Le Lez, S.; Arghir, M.; Frêne, J. Nonlinear Numerical Prediction of Gas Foil Bearing Stability and Unbalanced Response. *J. Eng. Gas Turbines Power* **2009**, *131*, 012503. [CrossRef]
7. Hoffmann, R.; Liebich, R. Characterisation and calculation of nonlinear vibrations in gas foil bearing systems–An experimental and numerical investigation. *J. Sound Vib.* **2018**, *412*, 389–409. [CrossRef]
8. Hoffmann, R.; Liebich, R. Experimental and numerical analysis of the dynamic behaviour of a foil bearing structure affected by metal shims. *Tribol. Int.* **2017**, *115*, 378–388. [CrossRef]
9. Ghalayini, I.; Bonello, P. A parametric study into the effect of variability in clearance shape and bump foil stiffness distribution in foil-air bearings. In Proceedings of the 12th Virtual Conference on Vibrations in Rotating Machinery (VIRM), London, UK, 14–15 October 2020. [CrossRef]
10. Kim, T.H.; Andrés, L.S. Effects of a Mechanical Preload on the Dynamic Force Response of Gas Foil Bearings: Measurements and Model Predictions. *Tribol. Trans.* **2009**, *52*, 569–580. [CrossRef]
11. Mahner, M.; Bauer, M.; Schweizer, B. Numerical analyzes and experimental investigations on the fully-coupled thermo-elasto-gasdynamic behavior of air foil journal bearings. *Mech. Syst. Sig. Process.* **2021**, *149*, 107221. [CrossRef]
12. Park, J.; Kim, D.; Sim, K. Rotordynamic Analysis of Piezoelectric Gas Foil Bearings with a Mechanical Preload Control Based on Structural Parameter Identifications. *Appl. Sci.* **2021**, *11*, 2330. [CrossRef]
13. Lund, J.W. Calculation of Stiffness and Damping Properties of Gas Bearings. *J. Lubr. Technol.* **1968**, *90*, 793–803. [CrossRef]
14. Pronobis, T.; Liebich, R. Comparison of stability limits obtained by time integration and perturbation approach for Gas Foil Bearings. *J. Sound Vib.* **2019**, *458*, 497–509. [CrossRef]

15. Larsen, J.S.; Santos, I.F.; von Osmanski, S. Stability of rigid rotors supported by air foil bearings: Comparison of two fundamental approaches. *J. Sound Vib.* **2016**, *381*, 179–191. [CrossRef]
16. Bonello, P.; Pourashraf, T. A comparison of modal analyses of foil-air bearing rotor systems using two alternative linearisation methods. *Mech. Syst. Sig. Process.* **2022**, *170*, 108714. [CrossRef]
17. Bonello, P.; Pham, H.M. The efficient computation of the nonlinear dynamic response of a foil–air bearing rotor system. *J. Sound Vib.* **2014**, *333*, 3459–3478. [CrossRef]
18. Baum, C.; Hetzler, H.; Seemann, W. On the Stability of Balanced Rigid Rotors in Air Foil Bearings. In *Proceedings of the SIRM 2015—11th International Conference on Vibrations in Rotating Machines, Magdeburg, Deutschland, 23–25 February 2015*; Paper—ID 52/S; Ecker, H., Aufl, E., Eds.; Institut für Mechanik: Karlsruhe, Germany, 2015; p. 17.
19. Zhou, R.; Gu, Y.; Cui, J.; Ren, G.; Yu, S. Nonlinear dynamic analysis of supercritical and subcritical Hopf bifurcations in gas foil bearing-rotor systems. *Nonlinear Dyn.* **2021**, *103*, 2241–2256. [CrossRef]
20. Khamari, D.S.; Kumar, J.; Behera, S.K. A Review on Modeling and Stability Aspects of Gas Foil Bearing Supported Rotors. *Tribol. Ind.* **2023**, *45*, 12–33. [CrossRef]
21. Walowit, J.A.; Anno, J.N.; Hamrock, B.J. Modern Developments in Lubrication Mechanics. *J. Lubr. Technol.* **1977**, *99*, 304–305. [CrossRef]
22. Heshmat, H.; Walowit, J.A.; Pinkus, O. Analysis of Gas-Lubricated Foil Journal Bearings. *J. Lubr. Technol.* **1983**, *105*, 647–655. [CrossRef]
23. Heshmat, H.; Walowit, J.A.; Pinkus, O. Analysis of Gas Lubricated Compliant Thrust Bearings. *J. Lubr. Technol.* **1983**, *105*, 638–646. [CrossRef]
24. Iordanoff, I. Analysis of an Aerodynamic Compliant Foil Thrust Bearing: Method for a Rapid Design. *J. Tribol.* **1999**, *121*, 816–822. [CrossRef]
25. Kim, D. Parametric Studies on Static and Dynamic Performance of Air Foil Bearings with Different Top Foil Geometries and Bump Stiffness Distributions. *J. Tribol.* **2007**, *129*, 354–364. [CrossRef]
26. Kim, T.H.; Andrés, L.S. Analysis of advanced gas foil bearings with piecewise linear elastic supports. *Tribol. Int.* **2007**, *40*, 1239–1245. [CrossRef]
27. Larsen, J.; Santos, I. Compliant Foil Journal Bearings—Investigation of Dynamic Properties. In Proceedings of the SIRM 2013: 10th International Conference on Vibrations in Rotating Machines, Berlin, Germany, 25–27 February 2013.
28. Peng, Z.; Khonsari, M. Hydrodynamic Analysis of Compliant Foil Bearings With Compressible Air Flow. *J. Tribol.* **2004**, *126*, 542–546. [CrossRef]
29. Schiffmann, J.; Spakovszky, Z.S. Foil Bearing Design Guidelines for Improved Stability. *J. Tribol.* **2012**, *135*. 011103. [CrossRef]
30. Bonello, P.; Hassan, M.B. An experimental and theoretical analysis of a foil-air bearing rotor system. *J. Sound Vib.* **2018**, *413*, 395–420. [CrossRef]
31. Larsen, J.S.; Santos, I.F. On the nonlinear steady-state response of rigid rotors supported by air foil bearings—Theory and experiments. *J. Sound Vib.* **2015**, *346*, 284–297. [CrossRef]
32. Kulkarni, S.; Radhakrishna, M.; Jana, S.; Kumar, V. Conical bump foil bearings for combined axial and radial load applications. In Proceedings of the International Symposium on Air Breathing Engines, Busan, Republic of Korea, 9–13 September 2013.
33. Sheng-Bo, L.; Savin, L.A.; Sytin, A.V.; Tyurin, V.O. Load capacity of foil gas dynamic bearings with conical surfaces lubricated with low-viscosity cryogenic fluids. In Proceedings of the International Scientific Conference BALTTRIB 2019, Kaunas, Lithuania, 14–16 November 2019; Volume 1, pp. 223–230. [CrossRef]
34. Hu, H.; Feng, M.; Ren, T. Study on the performance of novel gas foil conical bearings. *Proc. Inst. Mech. Eng. Part J J. Eng. Tribol.* **2021**, *235*, 883–900. [CrossRef]
35. Hu, H.; Feng, M. Design guidelines for bump-type compliant conical foil bearing. *Proc. Inst. Mech. Eng. Part C J. Mech. Eng. Sci.* **2021**, *236*, 956–971. [CrossRef]
36. Hu, H.; Feng, M.; Ren, T. Effect of roundness error on the performance of novel gas foil conical bearings. *Ind. Lubr. Tribol.* **2020**, *72*, 895–904. [CrossRef]
37. Hu, H.; Feng, M.; Ren, T. Effect of taper error on the performance of gas foil conical bearing. *Ind. Lubr. Tribol.* **2020**, *72*, 1189–1197. [CrossRef]
38. Hu, H.; Feng, M.; Ren, T. On the characteristics of gas foil conical bearings considering misalignment. *Ind. Lubr. Tribol.* **2021**, *73*, 126–136. [CrossRef]
39. J. Bootsma. Liquid-Lubricated Spiral-Groove Bearings. Ph.D. Thesis, Technische Universiteit Delft, Delft, The Netherlands, 1975.
40. Hamrock, B.J.; Schmid, S.R.; Jacobson, B.O. *Fundamentals of Fluid Film Lubrication*; McGraw-Hill Series in Mechanical Engineering; Marcel Dekker: New York, NY, USA, 2004.
41. Michel, H.; Liebich, R. Challenges in Validating a Thermo-Hydrodynamic Gas Foil Bearing Model. *J. Eng. Gas Turbines Power* **2021**, *143*, 041029. [CrossRef]
42. Kim, H.; Jang, G.; Ha, H. A generalized Reynolds equation and its perturbation equations for fluid dynamic bearings with curved surfaces. *Tribol. Int.* **2012**, *50*, 6–15. [CrossRef]

43. Agrawal, G.L. Analysis of Power-Shaped Multipad Hydrodynamic Conical Gas Bearings. *Tribol. Trans.* **1993**, *36*, 240–248. [CrossRef]
44. Nielsen, B.B.; Santos, I.F. Transient and steady state behaviour of elasto–aerodynamic air foil bearings, considering bump foil compliance and top foil inertia and flexibility: A numerical investigation. *Proc. Inst. Mech. Eng. Part J J. Eng. Tribol.* **2017**, *231*, 1235–1253. [CrossRef]